

1 Swelling effect on coal micro structure and associated 2 permeability reduction

3 Yihuai Zhang ^{a*}, Maxim Lebedev ^b, Mohammad Sarmadivaleh ^a, Ahmed Barifcani ^a, Taufiq Rahman ^a, and
4 Stefan Iglauer ^a

5 ^a *Department of Petroleum Engineering, Curtin University, 26 Dick Perry Avenue, 6151 Kensington, Australia*

6 ^b *Department of Exploration Geophysics, Curtin University, 26 Dick Perry Avenue, 6151 Kensington, Australia*

7
8 * corresponding author (yihuai.zhang@postgrad.curtin.edu.au)

9 10 **Abstract**

11 Porosity and permeability of deep unmineable coal seams are key parameters in the context
12 of (enhanced) coalbed methane recovery and CO₂ geo-storage in coal beds as they determine
13 productivity and injection rate. Porosity and permeability are again determined by the micro-
14 structure of the coal, and the cleat network-coal matrix system. Furthermore, it is well
15 established that swelling of the coal matrix due to water adsorption can significantly reduce
16 permeability. However, the exact effect of swelling due to water adsorption on the coal
17 micro-structure is only poorly understood, and how this microstructural change impacts on
18 the permeability and porosity characteristics of the coal. We thus imaged dry coal plugs and
19 swollen coal plugs (swollen due to brine adsorption) at high resolution (3.43 μm)³ in 3D with
20 an X-ray micro-computed tomograph (microCT). On the microCT images two types of cleats
21 were identified; cleats in the coal matrix and cleats syngeneic with the mineral phase.
22 Approximately 80% of the coal matrix cleats closed upon water adsorption, while the cleats
23 in the mineral phase were not affected. This cleat closure by water adsorption dramatically

24 reduced porosity and particularly permeability, consistent with dynamic permeability core-
25 flood measurements.

26

27 *Keywords: coal; swelling; cleat; microCT; porosity; permeability.*

28

29 **1. Introduction**

30 Coalbed methane recovery (CBM) has gained substantial interest in recent years. Essentially
31 CBM is a method to produce natural gas from deep unmineable coal seams, and it utilizes
32 pressure-driven fluid flow for hydrocarbon recovery, often in combination with hydraulic
33 fracturing [1] or N₂/CO₂ injection for enhanced production (ECBM) [2, 3]. However, the coal
34 permeability is dramatically reduced by several orders of magnitude [4, 5] due to water [6, 7]
35 or gas [8, 5] adsorption, which cause coal swelling and seriously limits the application of this
36 technology [8]. Water adsorption, on which we focus here, has also been suggested to
37 decrease the sorption capacity of CO₂/CH₄/N₂ in CBM/ECBM and storage volume for CO₂
38 geo-sequestration [9,10]. Water encroachment and associated water adsorption, however, is
39 natural during CBM/ECBM and CO₂ storage in coal seams [11].

40

41 To address these issues and to predict CBM production, several coal swelling – permeability
42 models were built, and the swelling characteristics are typically simulated by coal matrix
43 strain change (e.g. [12], [13]). However, these models failed to explain stress controlled
44 swelling laboratory test results [14] and thus newer strain model [15] have been tuned to
45 match the laboratory results. These models, however, still have significant limitations with
46 respect to predicting the effect of water swelling on porosity and permeability. Specifically,
47 these models treat the swelling effect as independent of the fracture system, i.e. the cleats are

48 fixed or only change due to effective stress changes; while it has been suggested that swelling
49 may close the cleats and thus reduce permeability [16, 17, 18].

50

51 Thus to fully understand the cleat system is of vital importance. Note that typically macro
52 cleats and micro cleats ($< 20 \mu\text{m}$), on which we focus here, are distinguished. Such micro
53 cleats have been analysed with medical x-ray computed tomography (medicalCT) (e.g. [19,
54 20]) and SEM (e.g. [21-24]). However, medicalCT has a relatively low resolution ($\sim 500 \mu\text{m}$)³
55 [25] and the coal microstructure (i.e. micro cleat system) cannot be resolved; while SEM
56 only produces 2D information of the sample surface, and that usually at vacuum conditions.
57 The detailed 3D morphological characteristics are, however, vital as 2D space has
58 significantly different fluid mechanical properties (e.g. the percolation threshold is much
59 lower in 3D than in 2D, [26]). More recently, x-ray micro-computed tomography (microCT)
60 – which has a significantly higher resolution than medicalCT - has been increasingly used in
61 petrophysical studies (e.g. compare the reviews by [27], [28] or [29] or for example [30],
62 [31]), and the micro structure of coal was imaged (e.g. [24], [32], [33]). However, there is a
63 serious lack of information regarding the effects of water swelling on the microstructure. We
64 thus now expanded on this microCT analysis and investigated how water swelling influences
65 the 3D morphology of coal at the micro-meter level.

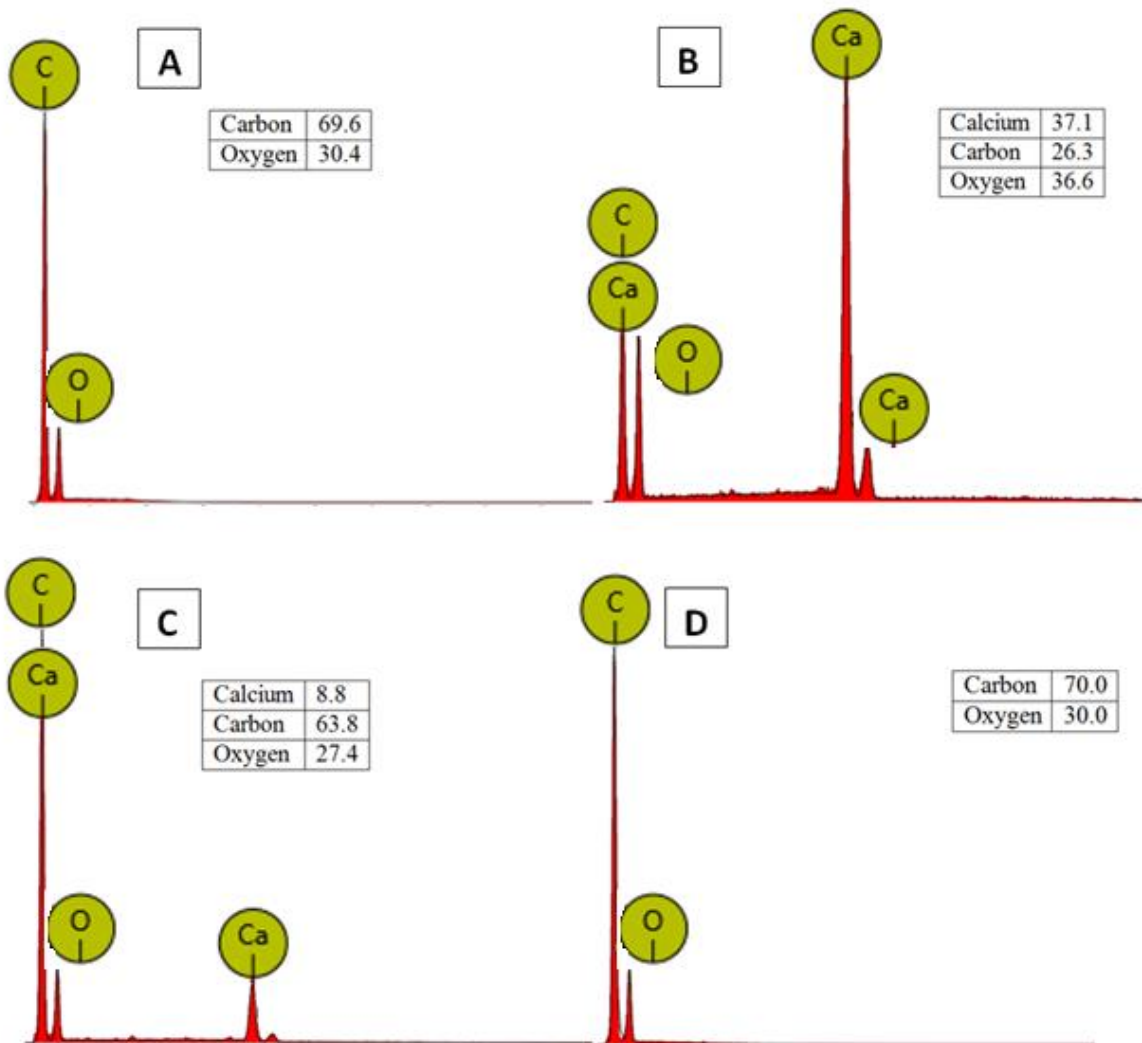
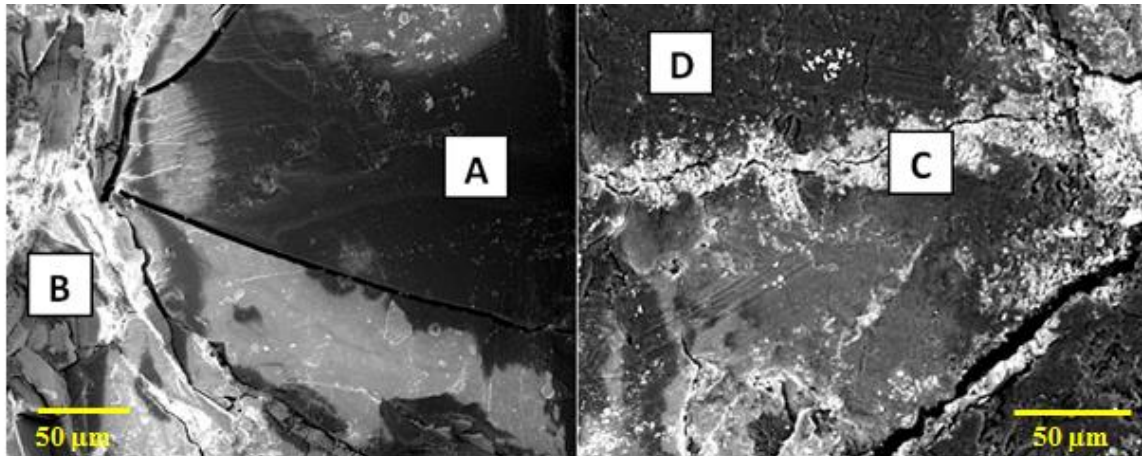
66

67 **2. Experimental Methodology**

68 *2.1. Materials*

69 A coal block was acquired from a depth of 750m in the Pingdingshan Ten coal mine, Henan
70 Province of China. The coal was a typical sub-bituminous coal (medium rank) with carbon
71 content $54(\pm 2) \%$ and volatile matter content $36(\pm 1) \%$, measured by Chinese Standards
72 GB/T 212-2008 and DL/T 1030-2006. Stripes of white minerals were identified visually with

73 sporadic distribution on the coal sample surface. Small samples were cut from adjacent
74 positions from the block, and subjected to SEM and EDS analysis, Fig. 1. The coal had a
75 relatively high oxygen content (~30 wt%; cp. points A and D in Fig. 1); the minerals were
76 identified as CaCO_3 (cp. points B and C in Fig. 1). Furthermore, a small dry coal plug (5mm
77 diameter, 10 mm length) was cut, again from the same block and a position adjacent to the
78 other samples, and this plug (Sample A) was imaged with an x-ray micro-computed
79 tomography (Xradia Versa-XRM) at a high resolution of $(3.43 \mu\text{m})^3$. X-ray accelerating
80 voltage was chosen as 40 kV, the x-ray beam size was approximately $0.3 \mu\text{m}$, and a 1000 x
81 1000 pixel detector was used for radiograph acquisition Total time for 3D imaging of the
82 sample was ~ 4 hours.



83

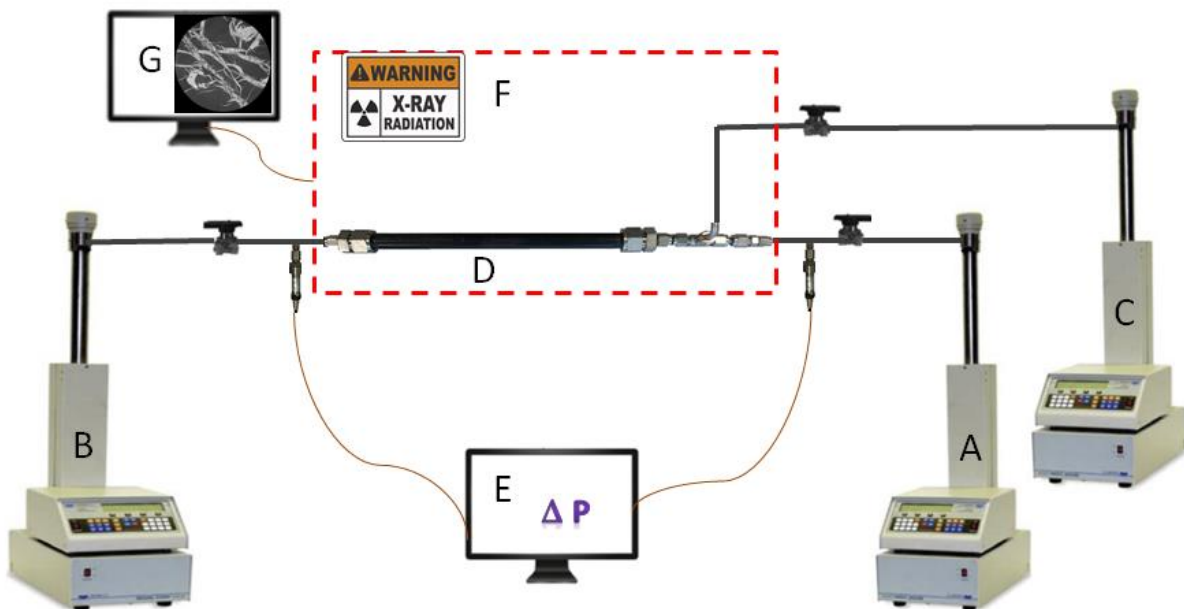
84 **Fig. 1.** SEM images of the coal sample with elemental compositions (wt % measured by
 85 EDS) for different points A, B, C and D indicated.

86

87 2.2 Permeability measurements and image processing

88 An experimental core flood apparatus was built for gas and brine permeability measurements
89 (Fig. 2). The small coal plug was mounted into an X-ray transparent flow cell, and the whole
90 apparatus was vacuumed for 12 hours to ensure that there is no air inside the plug sample or
91 the tube system. A confining pressure of 5 MPa was applied, and subsequently more than
92 7000 pore volumes (PV) of brine (5 wt% NaCl in deionized water) were injected at a flow
93 rate of 0.02 mL/min through the plug with a high precision syringe pump (Teledyne ISCO
94 500D) at 296 K; and the pressure drop across the plug was continuously measured with high
95 accuracy pressure sensors (Keller PAA-33X, accuracy 0.1%). Permeability was then
96 calculated using Darcy's law. This test was repeated thrice to test repeatability; all the three
97 samples (Sample A, Sample B and Sample C) were cut from the same coal block.

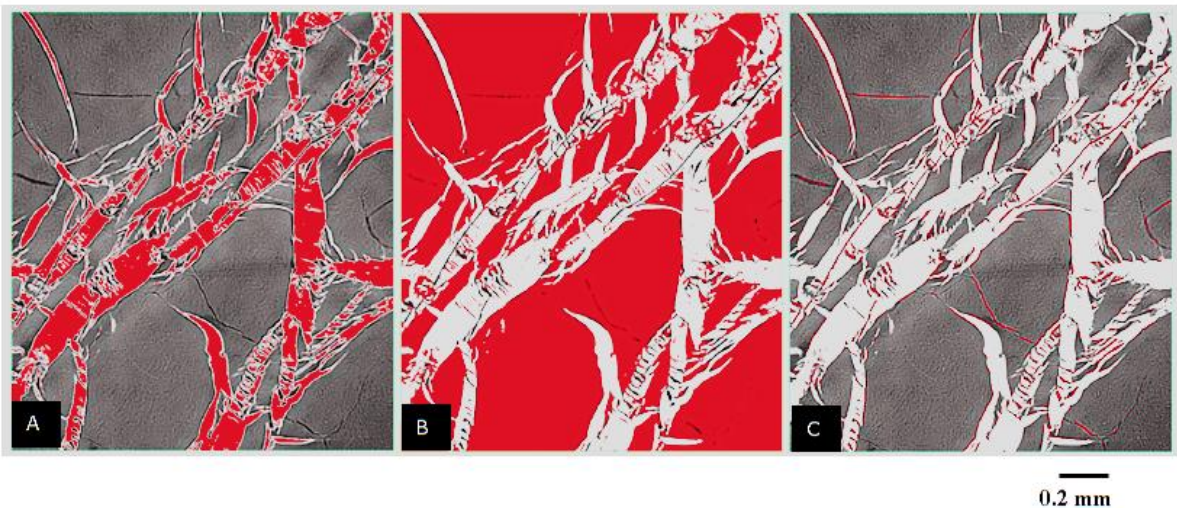
98



99

100 **Fig. 2.** Experimental apparatus used; (A) injection pump, (B) production pump, (C) confining
101 pressure pump, (D) core holder, (E) pressure data acquisition, (F) microCT, (G) microCT
102 images processing.

103 Injection was stopped after ~120 hours flooding time (when the permeability reduced by >
104 80%, Fig. 11), and the brine saturated plug was microCT imaged again at the same high
105 resolution (without confining stress). . Note that the plug was mechanically fixed inside the
106 microCT cell; thus the same sample volume was imaged. All microCT images were filtered
107 with a non-local means filter [34] and segmented with a watershed algorithm [35] [36] Fig. 3.



108

109 **Fig. 3.** Axial slices through the segmented microCT coal sample image: (A) calcium
110 carbonate minerals (red), (B) coal matrix (red), (C) micro cleats (red).

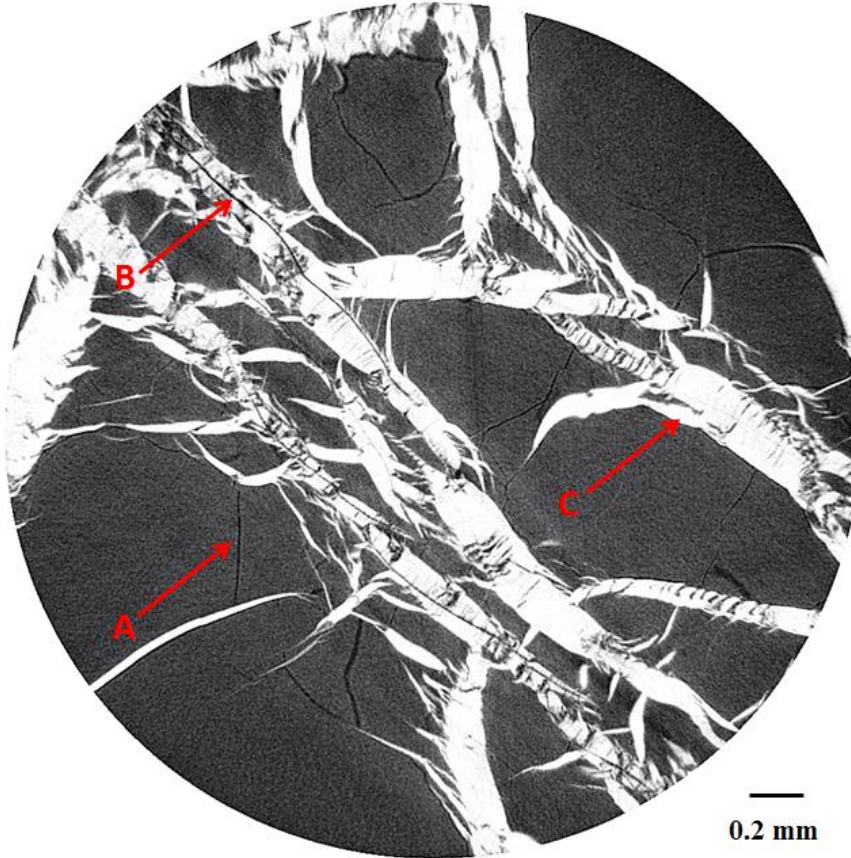
111

112 **3. Results and Discussion**

113 *3.1 Microstructure characteristics and segmented phases*

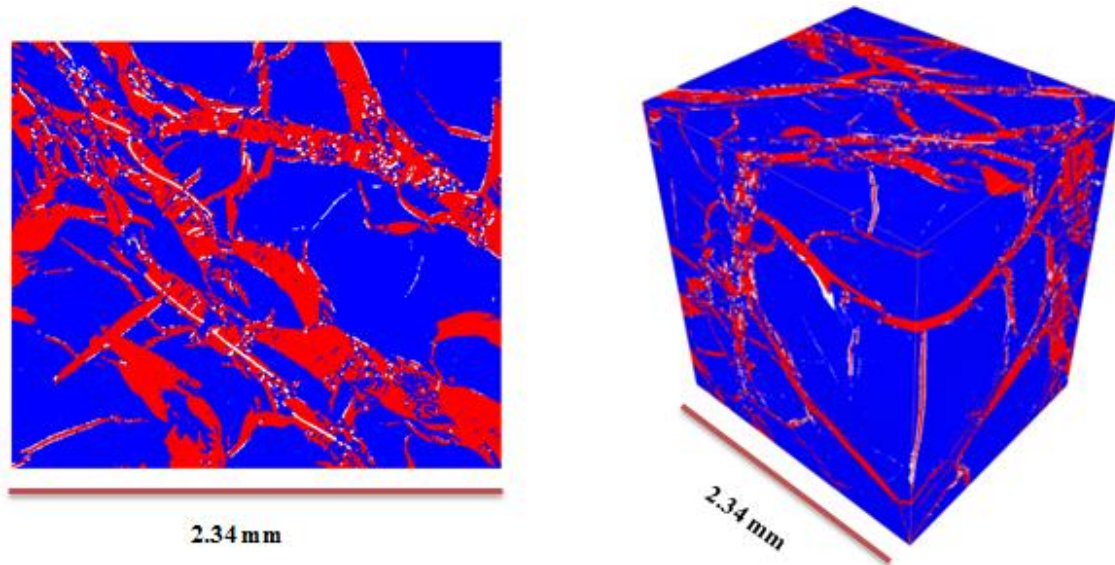
114 Three phases were clearly identified in the raw and segmented 2D/3D microCT images:
115 micro cleats (black), coal matrix (grey) and minerals (white) in raw images (Fig. 4a); with
116 white, blue and red in the segmented images (Fig. 4b). The widths of the micro cleats in the
117 dry plug were 5-10 μm (no confining stress), while lengths up to 2 mm were measured. These
118 micro-cleats can be divided into two groups according to their location in the sample: they

119 can be a) in the coal matrix (e.g. A in Fig. 4a or A in Fig. 1) or b) in the mineral phase (e.g. B
120 in Fig. 4a or C in Fig. 1). Clearly, the coal sample's microstructure is highly heterogeneous.



121

122 **Fig. 4a.** Axial 2D slice through the dry coal (3.43 μm resolution; raw image); the different
123 features can be clearly identified: (A) micro cleat in the coal matrix, (B) cleat inside mineral,
124 (C) mineral phase.



125

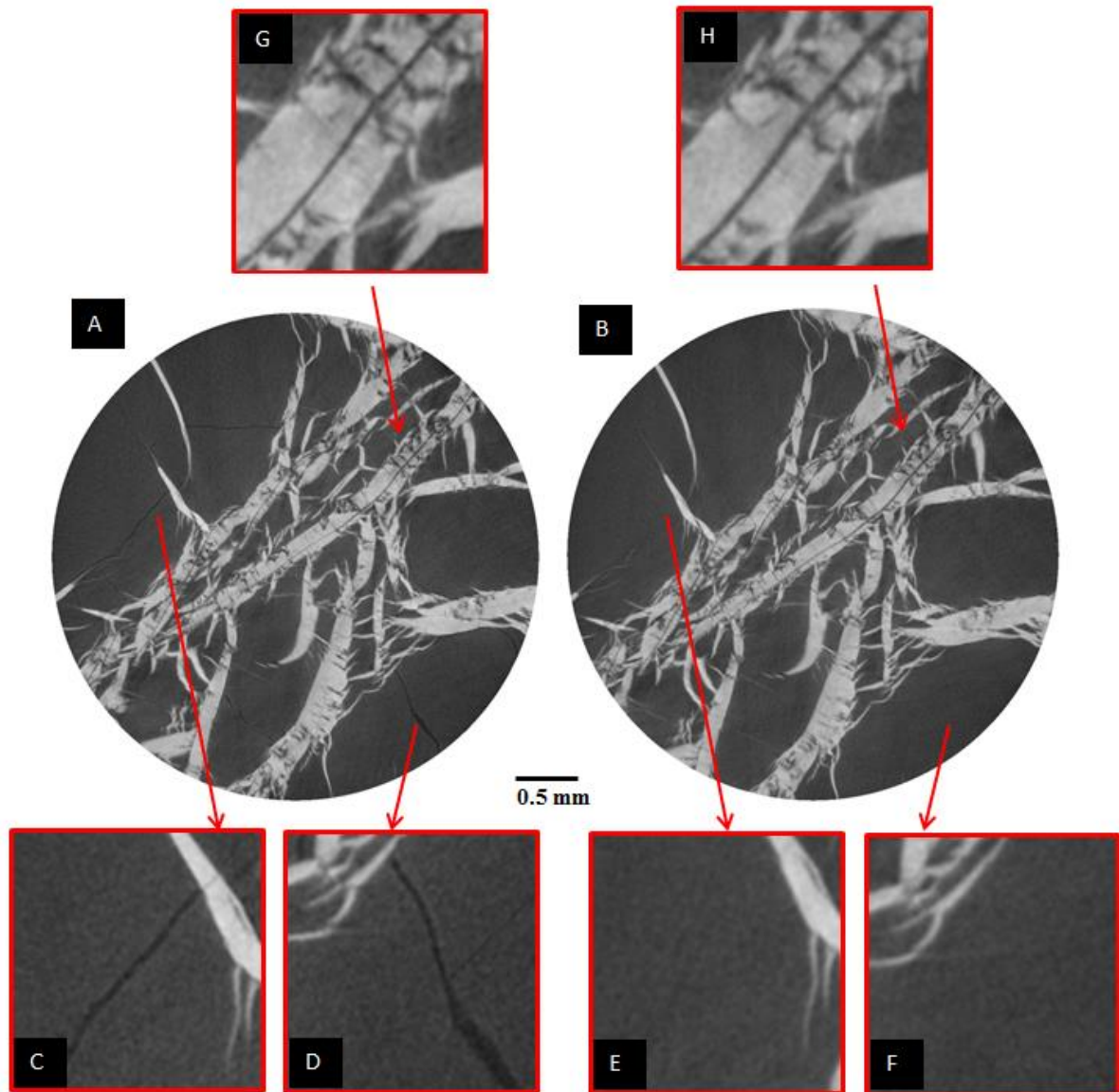
126 **Fig. 4b.** 2D and 3D views of the segmented coal sample; three phases were identified: micro
127 cleats (white); mineral phase (red); and coal matrix (blue).

128

129 3.2 *Microstructure evolution due to swelling*

130 3.2.1 *Qualitative analysis*

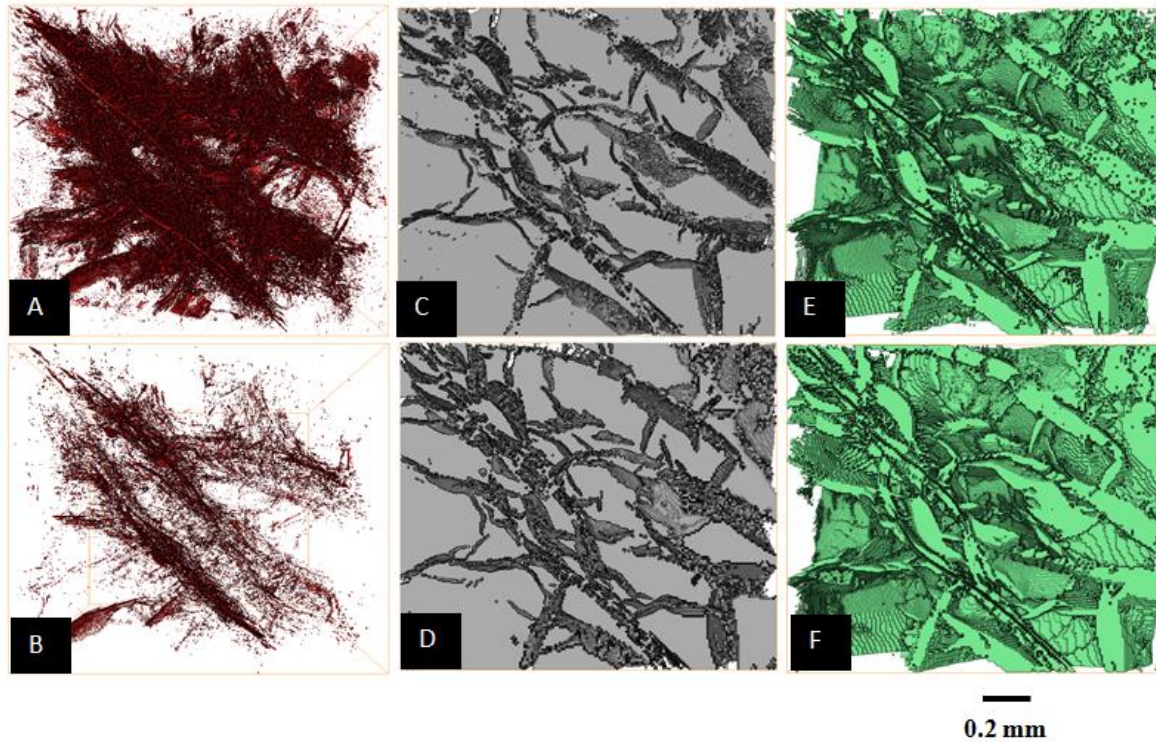
131 A clear change in the micro-structure was observed on the microCT images before and after
132 swelling (Fig. 5). Essentially the cleats in the coal matrix disappeared after the sample was
133 saturated with brine. However, no significant change was observed in terms of the mineral
134 phase and the cleats inside the mineral phase. In this context the concept of “internal
135 swelling stress” was proposed [37]; essentially, the coal “internal swelling stress” closed the
136 cleats; at the same time, the mineral phase had no such “internal swelling stress” and it is less
137 compressible, thus the open cleats were protected from closure by the mineral phase. The
138 micro cleats and generally the pore volume decreased significantly when the sample was
139 saturated, this is clearer in the segmented images (Fig. 6). All these evidence indicated that
140 water absorption into the coal matrix and associated coal matrix swelling.



142

143 **Fig. 5.** Axial 2D image slices through the coal plug (raw image); (A) dry sample, (B) brine
 144 saturated sample (same slice), (C and D) zoomed-into image A: the cleats and minerals can
 145 be seen clearly, (E and F) the sample area as shown in C and D: the cleats disappeared but the
 146 mineral phase did not change, (G and H) the cleats inside minerals showed no change before
 147 and after brine saturation.

148



149

150 **Fig. 6.** 3D images of the three segmented phases; (A) micro cleats, dry plug; (B) micro cleats,
 151 brine saturated plug; (C) coal matrix (shown in grey), dry plug; (D) coal matrix, brine
 152 saturated plug; (E) mineral phase, dry plug; (F) mineral phase, saturated plug.

153

154 3.2.2 Quantitative analysis

155 The microCT images were further analysed and the volume fractions of the different phases
 156 were measured before and after brine saturation. The micro cleat volume shrank significantly
 157 (by ~ 75%) due to brine saturation, while the coal matrix volume increased by the same
 158 nominal amount, but the mineral fraction volume stayed approximately constant, Table 1.

159

160 **Table 1**

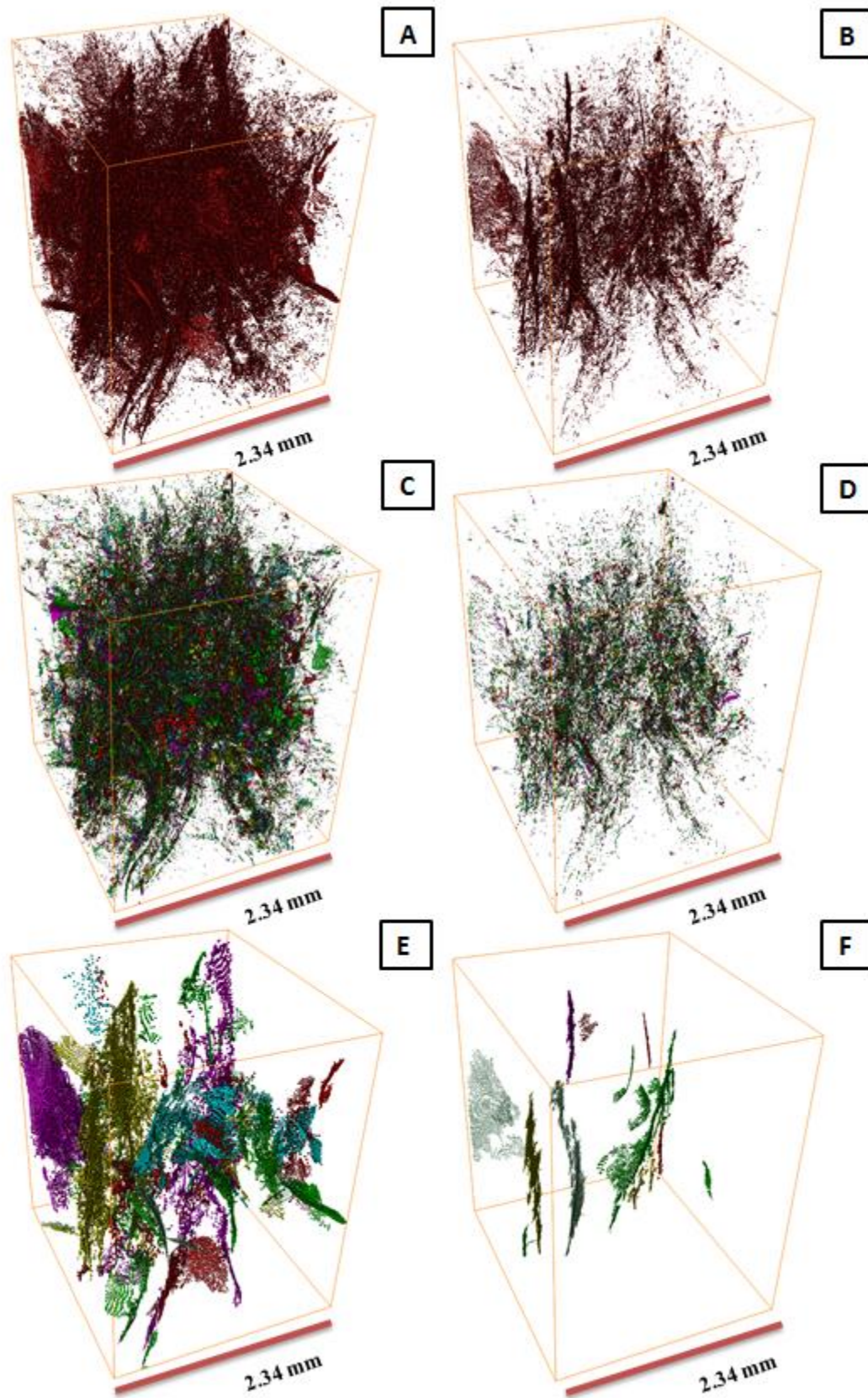
161 Volume fractions of the different phases in the coal plug measured on the micro-CT images.

| | Dry plug | Saturated plug |
|---|----------|----------------|
| Micro cleats total (%) | 2.85 % | 0.71 % |
| Micro cleats – Below threshold size (%) [*] | 1.20 % | 0.19 % |
| Micro cleats – Above threshold size (%) [*] | 1.65 % | 0.52 % |
| Minerals (%) | 28.79 % | 28.83 % |
| Coal matrix (%) | 68.36 % | 70.46 % |
| Effective cleat porosity [*] | 1.19 % | 0.19 % |

162 ^{*}Cross-sectional threshold value = 50000 μm^2 .

163

164 The 3D topographies (A and B in Fig. 7) illustrate how the micro cleats changed due to brine
165 saturation. The cross sectional area (μm^2) was chose as the threshold value which is better
166 description for the morphology of cleats (thin and long) than the volume (μm^3) value, We
167 further divided small micro cleats (C and D in Fig. 7; all void cross-sectional areas ≤ 50000
168 μm^2) and larger micro cleats (E and F in Fig. 7) for better visualization; all void space
169 significantly shrank due to brine saturation, furthermore almost all larger micro cleats were
170 oriented vertically where along the coal bed. The absolute porosity (ϕ) for each image slice
171 was computed, and ϕ was clearly reduced by swelling throughout the plug (Fig. 8). We
172 further analysed the effective porosity (ϕ_e); ϕ_e also dramatically decreased (from 1.19 % to
173 0.19 %). This is consistent with our pore size distribution measurements on the microCT
174 images: all micro-cleats shrank, particularly the larger ones (Fig. 9). Finally we extracted a
175 pore network for the dry and brine saturated plug with a skeletonization algorithm [38],
176 Figure 10; clearly the number of fluid conduits was significantly reduced by brine saturation.

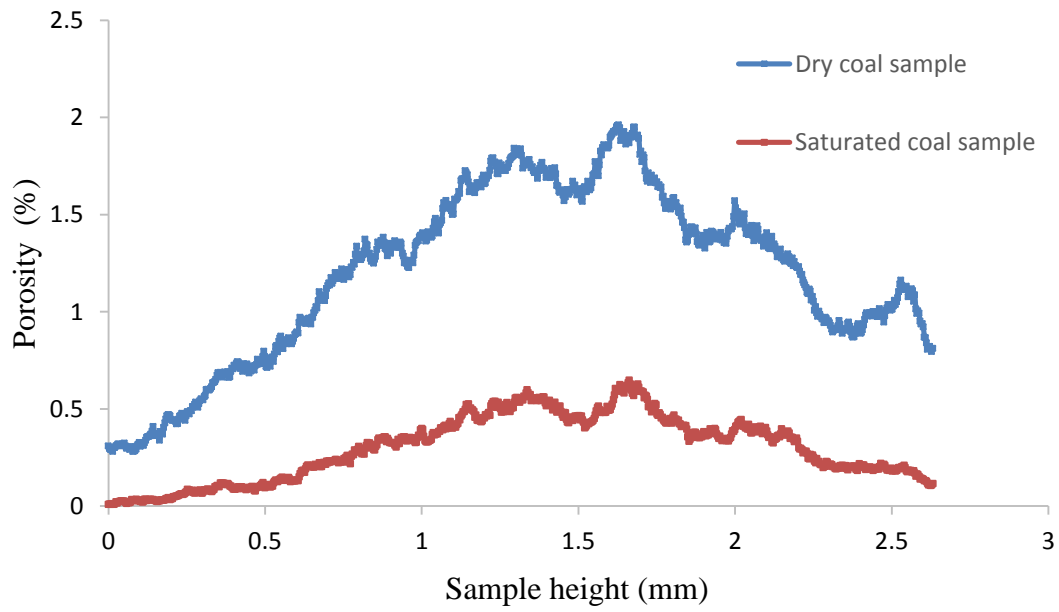


177

178 **Fig. 7.** 3D visualization of the micro cleat system before (left) and after (right) brine
 179 saturation; a threshold value of $50000 \mu\text{m}^2$ was set for the cleat cross-sectional area to

180 distinguish smaller and larger cleats; (A) micro cleats, dry sample; (B) micro cleats, brine
181 saturated plug; (C) micro cleats ($\leq 50000 \mu\text{m}^2$), dry sample; (D) micro cleats ($\leq 50000 \mu\text{m}^2$),
182 saturated plug; (E) micro cleats ($> 50000 \mu\text{m}^2$), dry sample; (F) micro cleats ($> 50000 \mu\text{m}^2$),
183 saturated plug.

184

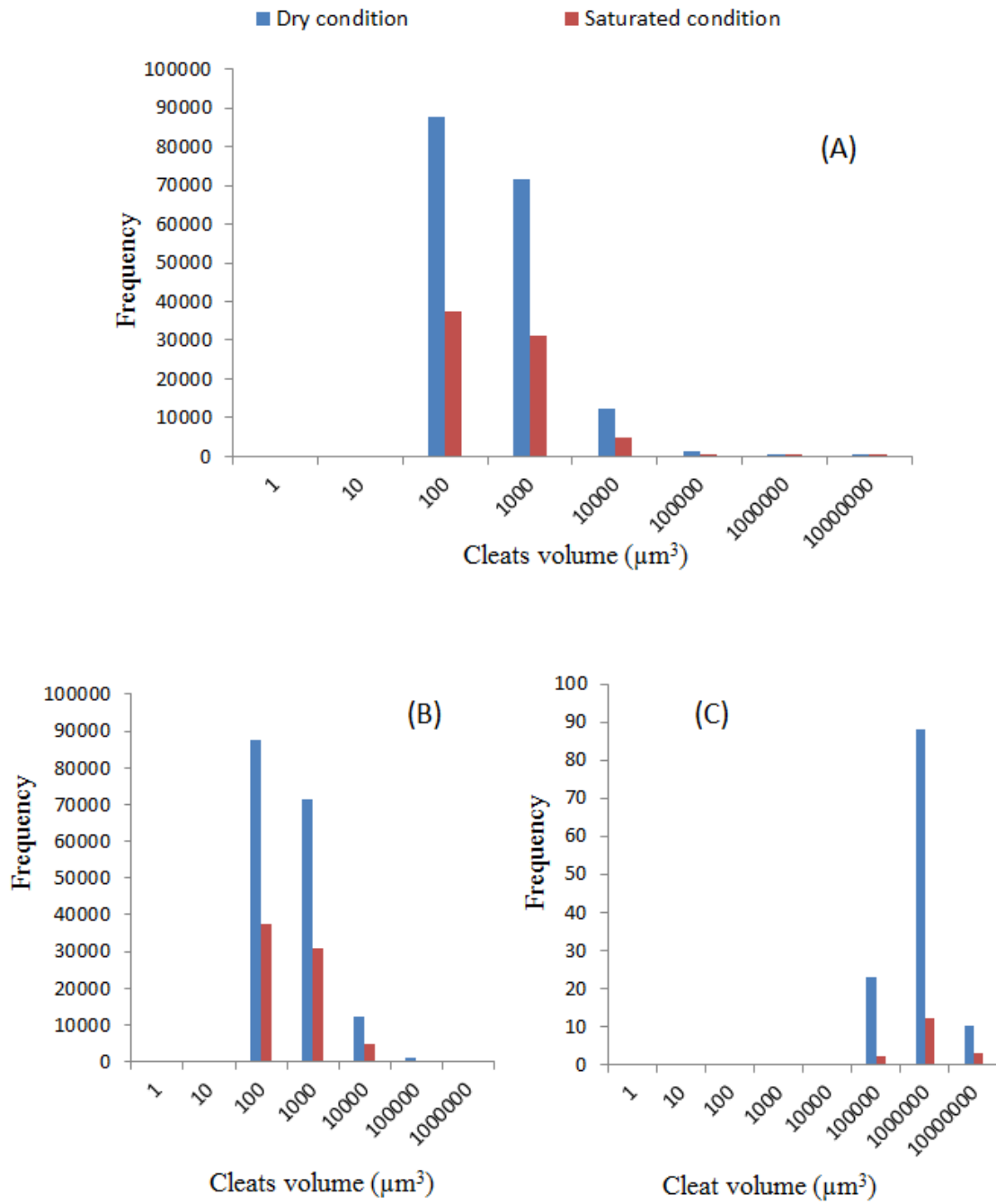


185

186

Fig. 8. Porosity versus sample height.

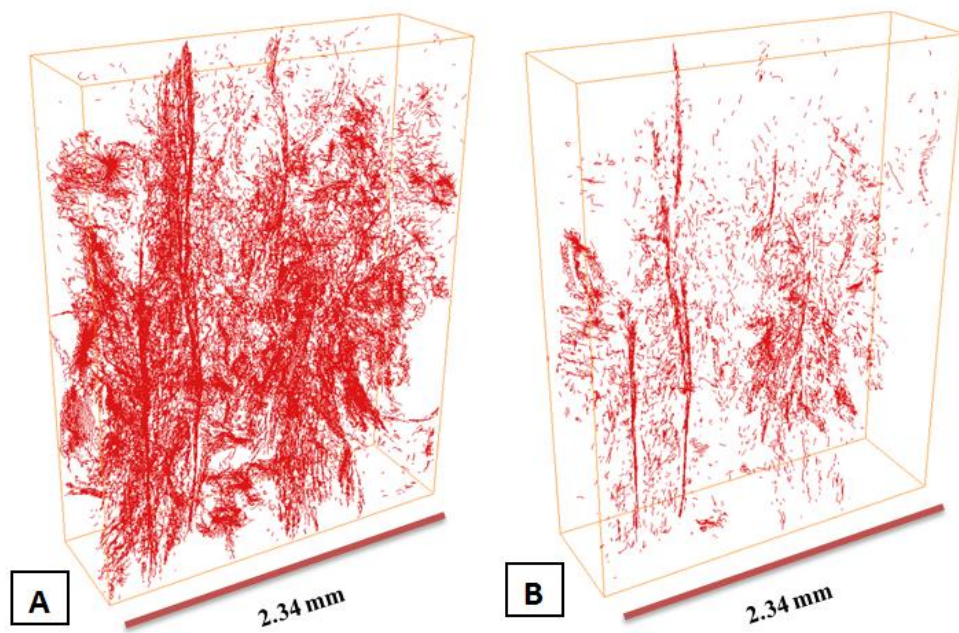
187



188

189 **Fig. 9.** Cleat size distributions before and after swelling (caused by brine saturation); (a) all
 190 cleats; (b) cleats $\leq 50000 \mu\text{m}^2$; (c) cleats $> 50000 \mu\text{m}^2$. $50000 \mu\text{m}^2$ is the threshold value of
 191 cross-sectional void area.

192



193

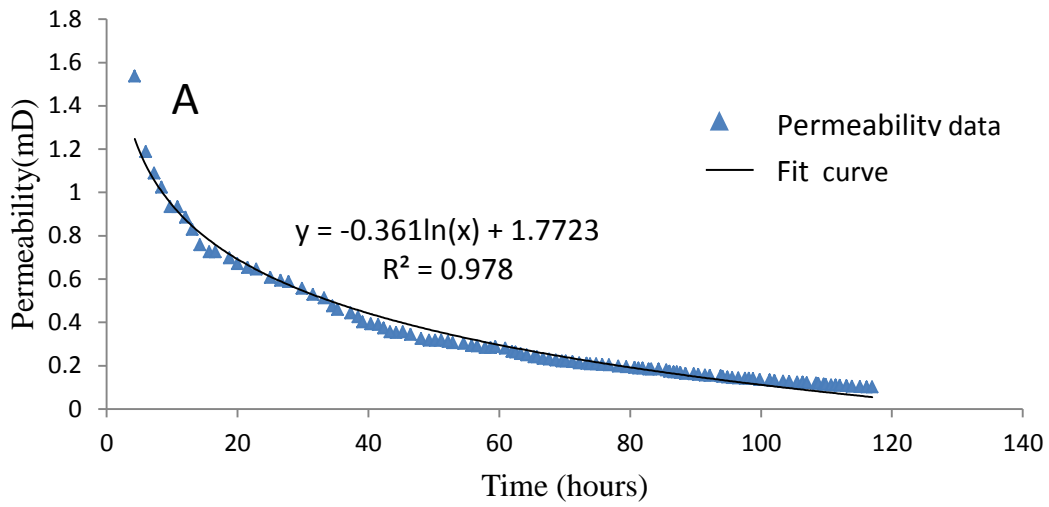
194 **Fig. 10.** Pore networks extracted by skeletonization algorithm [38], no confining stress; (A)
195 dry coal sample; (B) brine saturated coal sample.

196

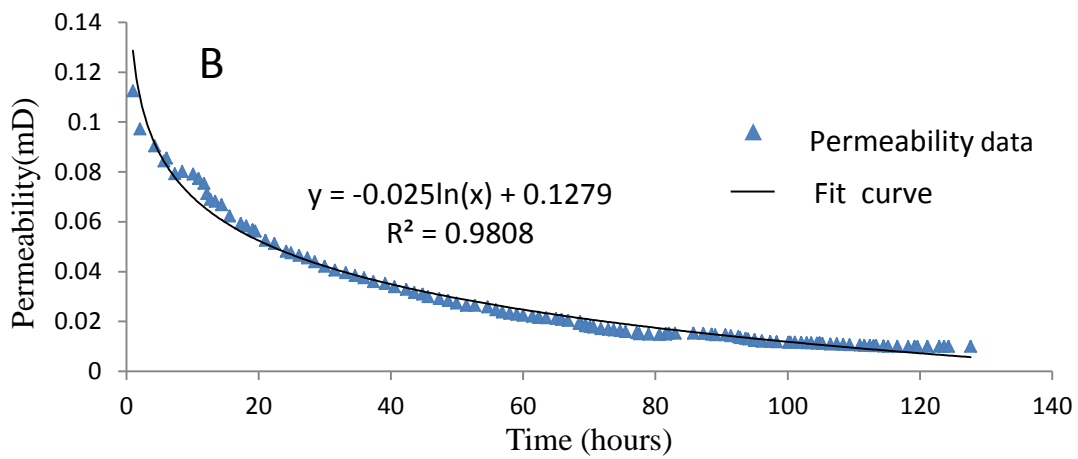
197 3.3 Permeability evolution

198 The dynamic permeability during brine injection was measured on three separate plugs
199 (Sample A, B and C), see above in the methodology section. Permeability consistently
200 dropped rapidly in the first 60 hours of the experiment (~ 3700 PV of brine injected), Figure
201 11. This permeability drop can be fitted with logarithmic curves (printed onto the graphs in
202 Fig. 11). However, the plugs had significantly different absolute permeabilities; which is
203 expected as coal is a rather heterogeneous material (cp. section 3.1). The graphs were quite
204 similar though, all samples underwent a >80% permeability loss after injection of ~ 7300 PV
205 of brine. This permeability drop is consistent with the microCT analysis above: porosity
206 significantly reduced during the water absorption process (from 2.85% to 0.81%); and

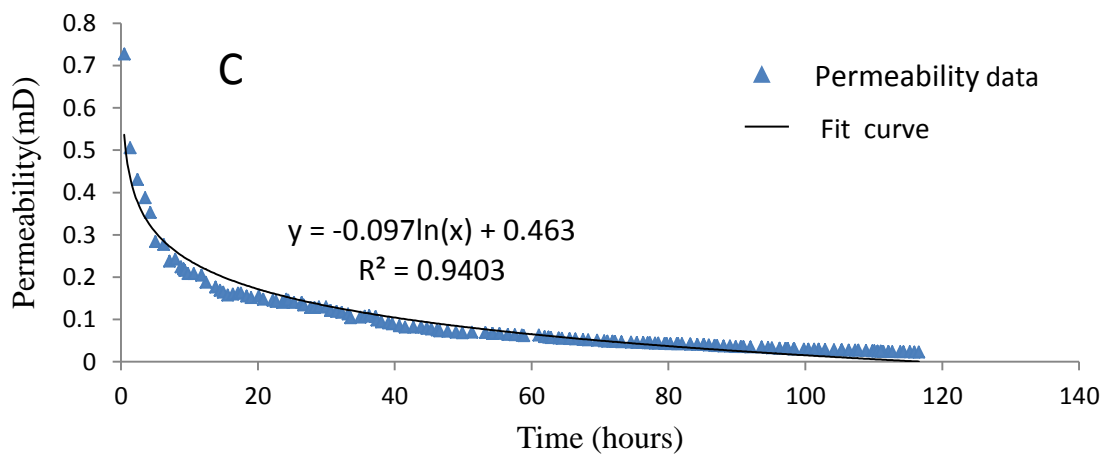
207 permeability loss was caused by closure of 80% of the micro cleats (cp. Fig. 10), which was
208 induced by coal matrix swelling.



209



210



211

212

213 **Fig. 11.** Dynamic permeability versus brine injection time for the three coal samples tested
214 (confining stress = 5 MPa), brine was injected at a flow rate of 0.02 mL/min (i.e. 100h
215 correspond to ~6200 PV of brine injected); A for sample A, B for sample B and C for sample
216 C.

217

218 **4. Conclusions**

219 Coal porosity and permeability are key parameters as they control natural gas production
220 from deep (unmineable) coal seams [39, 40, 41]. However, the microstructure of the coal –
221 which ultimately determines coal porosity and permeability – is only poorly understood. This
222 is especially true for the effect of swelling on the microstructure (e.g. [42]) – which is a well-
223 known cause for permeability change (e.g. [17])

224

225 Thus we imaged dry and swollen (due to brine absorption) coal plugs with 3D microCT at a
226 high voxel resolution ($3.4 \mu\text{m}$)³. The dry images were similar to those acquired by [33] and
227 [24]; and the medium rank coal was highly heterogeneous and had a low porosity ($2.85 \% \pm$
228 1%) and permeability ($\sim 0.1 \text{ mD} - 10 \text{ mD}$) and a significant mineral content. Micro cleats were
229 visible in the coal matrix and the mineral phase, consistent with SEM imaging (cp. Fig. 1).
230 However, when brine was injected into a dry coal plug, more than 80% of these cleats closed
231 due to swelling, which caused a dramatic reduction in porosity and particularly permeability.
232 But the cleats in the mineral phase were still open after the coal matrix swelling; this could be
233 explained by the lower internal stress in the mineral and the lower compressibility of the
234 mineral.

235

236 We conclude that water absorption into dry coal causes significant swelling effects. This
237 swelling drastically alters the microstructure of the coal; which again drastically reduces coal
238 permeability.

239

240 **Acknowledgment**

241 The authors thank the National Geosequestration Laboratory (NGL) of Australia for
242 providing access to the X-ray microscope VersaXRM-500 (Zeiss-Xradia) . Funding for this
243 facility was provided by the Australian Federal Government.

244

245 **References**

- 246 [1] S. Holditch, J. Ely, M. Semmelbeck, R. Carter, J. Hinkel, R. Jeffrey Jr, Enhanced recovery of coalbed
247 methane through hydraulic fracturing, in: SPE Annual Technical Conference and Exhibition, Society
248 of Petroleum Engineers, 1988.
- 249 [2] S.R. Reeves, Geological Sequestration of CO₂ in Deep, Unmineable Coalbeds: An Integrated
250 Research and Commerical-Scale Field Demonstration Project, in: SPE annual technical conference
251 and exhibition, Society of Petroleum Engineers, 2001.
- 252 [3] S. Reeves, D. Davis, A. Oudinot, A technical and economic sensitivity study of enhanced coalbed
253 methane recovery and carbon sequestration in coal, DOE topical report, (2004).
- 254 [4] L. Pekot, S. Reeves, Modeling the effects of matrix shrinkage and differential swelling on coalbed
255 methane recovery and carbon sequestration, in: Paper 0328, proc. 2003 International Coalbed
256 Methane Symposium. University of Alabama, Citeseer, 2003.
- 257 [5] J. Shi, S. Durucan, CO₂ storage in deep unminable coal seams, Oil & gas science and technology,
258 60 (2005) 547-558.
- 259 [6] P.L. Walker, S.K. Verma, J. Rivera-Utrilla, A. Davis, Densities, porosities and surface areas of coal
260 macerals as measured by their interaction with gases, vapours and liquids, Fuel, 67 (1988) 1615-
261 1623.
- 262 [7] D. Charrière, P. Behra, Water sorption on coals, Journal of colloid and interface science, 344
263 (2010) 460-467.
- 264 [8] S.R. Reeves, The Coal-Seq project: Key results from field, laboratory and modeling studies, in:
265 Proceedings of the 7th International Conference on Greenhouse Gas Control Technologies (GHGT-7),
266 Citeseer, 2004, pp. 1399-1406.
- 267 [9] B. Krooss, F. Van Bergen, Y. Gensterblum, N. Siemons, H. Pagnier, P. David, High-pressure
268 methane and carbon dioxide adsorption on dry and moisture-equilibrated Pennsylvanian coals,
269 International Journal of Coal Geology, 51 (2002) 69-92.
- 270 [10] E. Ozdemir, K. Schroeder, Effect of moisture on adsorption isotherms and adsorption capacities
271 of CO₂ on coals, Energy & Fuels, 23 (2009) 2821-2831.

272 [11] S.H. Stevens, D. Spector, P. Riemer, Enhanced coalbed methane recovery using CO₂ injection:
273 worldwide resource and CO₂ sequestration potential, in: SPE International Oil and Gas Conference
274 and Exhibition in China, Society of Petroleum Engineers, 1998.

275 [12] S. Day, R. Fry, R. Sakurovs, Swelling of Australian coals in supercritical CO₂, International
276 Journal of Coal Geology, 74 (2008) 41-52.

277 [13] M. Vandamme, L. Brochard, B. Lecampion, O. Coussy, Adsorption and strain: the CO₂-induced
278 swelling of coal, Journal of the Mechanics and Physics of Solids, 58 (2010) 1489-1505.

279 [14] J. Liu, Z. Chen, D. Elsworth, H. Qu, D. Chen, Interactions of multiple processes during CBM
280 extraction: a critical review, International Journal of Coal Geology, 87 (2011) 175-189.

281 [15] Y. Peng, J. Liu, M. Wei, Z. Pan, L.D. Connell, Why coal permeability changes under free swellings:
282 New insights, International Journal of Coal Geology, 133 (2014) 35-46.

283 [16] J.W. Larsen, The effects of dissolved CO₂ on coal structure and properties, International Journal
284 of Coal Geology, 57 (2004) 63-70.

285 [17] S. Mazumder, A.A. Karnik, K.-H.A. Wolf, Swelling of coal in response to CO₂ sequestration for
286 ECBM and its effect on fracture permeability, Spe Journal, 11 (2006) 390-398.

287 [18] Z. Pan, L.D. Connell, A theoretical model for gas adsorption-induced coal swelling, International
288 Journal of Coal Geology, 69 (2007) 243-252.

289 [19] C.D. Montemagno, L.J. Pyrak-Nolte, Porosity of natural fracture networks, Geophysical Research
290 Letters, 22 (1995) 1397-1400.

291 [20] S. Mazumder, K.-H. Wolf, K. Elewaut, R. Ephraim, Application of X-ray computed tomography for
292 analyzing cleat spacing and cleat aperture in coal samples, International Journal of Coal Geology, 68
293 (2006) 205-222.

294 [21] R. Ye, C. Xiang, J. Lin, Z. Peng, K. Huang, Z. Yan, N.P. Cook, E.L. Samuel, C.-C. Hwang, G. Ruan,
295 Coal as an abundant source of graphene quantum dots, Nature communications, 4 (2013).

296 [22] B.G. Kutchko, A.L. Goodman, E. Rosenbaum, S. Natesakhawat, K. Wagner, Characterization of
297 coal before and after supercritical CO₂ exposure via feature relocation using field-emission scanning
298 electron microscopy, Fuel, 107 (2013) 777-786.

299 [23] F. Huggins, D. Kosmack, G. Huffman, R. Lee, Coal mineralogies by SEM automatic image analysis,
300 Scanning Electron Microsc.;(United States), 1980 (1980).

301 [24] H.L. Ramandi, P. Mostaghimi, R.T. Armstrong, M. Saadatfar, W.V. Pinczewski, Porosity and
302 permeability characterization of coal: a micro-computed tomography study, International Journal of
303 Coal Geology, 154 (2016) 57-68.

304 [25] V. Cnudde, B. Masschaele, M. Dierick, J. Vlassenbroeck, L. Van Hoorebeke, P. Jacobs, Recent
305 progress in X-ray CT as a geosciences tool, Applied Geochemistry, 21 (2006) 826-832.

306 [26] D. Stauffer, Scaling theory of percolation clusters, Physics reports, 54 (1979) 1-74.

307 [27] M.J. Blunt, B. Bijeljic, H. Dong, O. Gharbi, S. Iglauer, P. Mostaghimi, A. Paluszny, C. Pentland,
308 Pore-scale imaging and modelling, Advances in Water Resources, 51 (2013) 197-216.

309 [28] D. Wildenschild, A.P. Sheppard, X-ray imaging and analysis techniques for quantifying pore-scale
310 structure and processes in subsurface porous medium systems, Advances in Water Resources, 51
311 (2013) 217-246.

312 [29] V. Cnudde, M.N. Boone, High-resolution X-ray computed tomography in geosciences: A review
313 of the current technology and applications, Earth-Science Reviews, 123 (2013) 1-17.

314 [30] S. Iglauer, A. Paluszny, C.H. Pentland, M.J. Blunt, Residual CO₂ imaged with X-ray micro-
315 tomography, Geophysical Research Letters, 38 (2011).

316 [31] S. Iglauer, A. Paluszny, M. Blunt, Simultaneous oil recovery and residual gas storage: A pore-
317 level analysis using in situ X-ray micro-tomography, Fuel, 103 (2013) 905-914.

318 [32] Y. Yu, W. Liang, Y. Hu, Q. Meng, Study of micro-pores development in lean coal with
319 temperature, International Journal of Rock Mechanics and Mining Sciences, 51 (2012) 91-96.

320 [33] L.M. Pant, H. Huang, M. Secanell, S. Larter, S.K. Mitra, Multi scale characterization of coal
321 structure for mass transport, Fuel, 159 (2015) 315-323.

- 322 [34] A. Buades, B. Coll, J.-M. Morel, A non-local algorithm for image denoising, in: Computer Vision
323 and Pattern Recognition, 2005. CVPR 2005. IEEE Computer Society Conference on, IEEE, 2005, pp.
324 60-65.
- 325 [35] J.B. Roerdink, A. Meijster, The watershed transform: Definitions, algorithms and parallelization
326 strategies, *Fundamenta informaticae*, 41 (2000) 187-228.
- 327 [36] S. Schlüter, A. Sheppard, K. Brown, D. Wildenschild, Image processing of multiphase images
328 obtained via X-ray microtomography: a review, *Water Resources Research*, 50 (2014) 3615-3639.
- 329 [37] H.-H. Liu, J. Rutqvist, A new coal-permeability model: internal swelling stress and fracture-
330 matrix interaction, *Transport in Porous Media*, 82 (2010) 157-171.
- 331 [38] Z. Liang, M. Ioannidis, I. Chatzis, Geometric and topological analysis of three-dimensional porous
332 media: pore space partitioning based on morphological skeletonization, *Journal of colloid and
333 interface science*, 221 (2000) 13-24.
- 334 [39] J. Gale, P. Freund, Coal-Bed Methane Enhancement with CO₂ Sequestration Worldwide
335 Potential, *Environmental Geosciences*, 8 (2001) 210-217.
- 336 [40] H. Sharma, S. Mazumder, T. Gilbert, M. Tovar, J.A. Philpot, Novel Approach to EUR estimation in
337 Coal Seam Gas Wells, in: SPE Unconventional Resources Conference and Exhibition-Asia Pacific,
338 Society of Petroleum Engineers, 2013.
- 339 [41] M. Creech, B. McConachie, Reserve estimation and the influence of coal seams on coal seam gas
340 productivity, in, Australasian Institute of Mining and Metallurgy, 2014.
- 341 [42] A. Syed, S. Durucan, J.-Q. Shi, A. Korre, Flue Gas Injection for CO₂ Storage and Enhanced
342 Coalbed Methane Recovery: Mixed Gas Sorption and Swelling Characteristics of Coals, *Energy
343 Procedia*, 37 (2013) 6738-6745.